BNL-225500-2024-JAAM

Three-dimensional nanoscale metal, metal oxide, and semiconductor frameworks through DNA-programmable assembly and templating

A. Michelson

To be published in "Science Advances"

January 2024

Center for Functional Nanomaterials

Brookhaven National Laboratory

U.S. Department of Energy

USDOE Office of Science (SC), Basic Energy Sciences (BES). Scientific User Facilities (SUF)

DISCLAIMER

MATERIALS SCIENCE

Three-dimensional nanoscale metal, metal oxide, and semiconductor frameworks through DNA-programmable assembly and templating

Aaron Michelson[1,2], Ashwanth Subramanian[3], Kim Kisslinger[1], Nikhil Tiwale[1], Shuting Xiang[4], Eric Shen[4], Jason S. Kahn[1], Dmytro Nykypanchuk[1], Hanfei Yan[5], Chang-Yong Nam[1,3]*, Oleg Gang[1,2,4]*

Controlling the three-dimensional (3D) nanoarchitecture of inorganic materials is imperative for enabling their novel mechanical, optical, and electronic properties. Here, by exploiting DNA-programmable assembly, we establish a general approach for realizing designed 3D ordered inorganic frameworks. Through inorganic templating of DNA frameworks by liquid- and vapor-phase infiltrations, we demonstrate successful nanofabrication of diverse classes of inorganic frameworks from metal, metal oxide and semiconductor materials, as well as their combinations, including zinc, aluminum, copper, molybdenum, tungsten, indium, tin, and platinum, and composites such as aluminum-doped zinc oxide, indium tin oxide, and platinum/aluminum-doped zinc oxide. The open 3D frameworks have features on the order of nanometers with architecture prescribed by the DNA frames and self-assembled lattice. Structural and spectroscopic studies reveal the composition and organization of diverse inorganic frameworks, as well as the optoelectronic properties of selected materials. The work paves the road toward establishing a 3D nanoscale lithography.

INTRODUCTION

Modern technological advances in electronics, photonics, and sensing rely heavily on planar fabrication approaches offered by top-down lithographic methods (*1*). However, in a broad range of emerging applications in optical and mechanical metamaterials, neuromorphic computing and energy materials require three-dimensional (3D) framework organization with complex material compositions and controllable nanoscale architecture (*2*–*4*). Additive manufacturing provides a route for fabricating 3D structured metals at the microscales (*5*). At the nanoscales, multistep planar lithography and deposition methods have demonstrated a structural control with a resolution extending to ~30 to 100 nm. The technique, however, faces challenges of incorporating a broad class of materials as well as the effort-intensive and low-throughput fabrication of 3D architecture in the sub–30-nm range (*6*–*8*). On the other side, self-assembly approaches using surfactants, polymers, and biomolecules, and shaped nanoparticles offer a rich structural diversity in 3D (*9*–*14*) that can be combined with inorganic templating, which allows for fabrication parallelization. However, these approaches typically do not offer ways to prescribe specific nanoscale architecture, and the breadth of material systems is limited.

In the past decade, DNA-based assembly methods have been increasingly proven to be capable of organizing matter on the nanoscales (*15*–*19*), noted for the ability to precisely place inorganic and biological nano-objects according to the designed parameters of the desired structures. For example, DNA origami, due to its shape and interaction programmability as well as size matching with nano-objects, represents a versatile approach for rational generation of diverse structural motifs that can be self-assembled in larger-scale spatially organized 3D frameworks consisting of optical, magnetic, bioactive nano-objects. However, to exploit these 3D DNA-based nanomaterials, robustness and specific functionality are typically required. Converting these 3D frameworks into inorganic architectures might introduce the framework complexity to inorganic materials.

A DNA metallization through the adsorption of ions on a charged DNA backbone was extensively investigated for potential use in molecular electronics (*20*–*22*). However, this approach typically results in nucleation and unconstrained growth (*23*). Recent advances in the silication of complex DNA architectures expanded the potential use of DNA-assembled materials to applications requiring robustness against temperature, environmental factors, and radiation (*24*–*28*). Concerning material diversity, DNA was shown to template biologically inspired calcium phosphate growth (*29*), and processing of silica into silicon carbide was demonstrated for DNA frameworks, providing feasibility of creating a wide bandgap semiconductor (*30*). To enable a broad range of applications, these silica-based frameworks can be used as architected 3D supports to host other functionally active material coatings.

While thermal evaporation of niobium onto silica lattice framework was demonstrated for creating niobium 3D nanostructures with superconducting properties (*31*), this fabrication approach suffers from low penetration into the 3D structure. To overcome this limitation and to establish a broadly applicable platform for creating 3D frameworks of different classes of materials, a universal strategy for 3D inorganic templating is needed. It has been shown that silica gel can be used for the sorption of metal ions from solution for a large range of metal salts (*32*). Overall, this suggested that at low pH, sorption to the silica follows the law of mass action.

Ex situ organic-inorganic hybridization techniques, including liquid-phase infiltration (LPI) and vapor-phase infiltration (VPI), are emerging as new methods for converting polymer templates into

[1]Center for Functional Nanomaterials, Brookhaven National Laboratory, Upton, NY 11973, USA. [2]Department of Applied Physics and Applied Mathematics, Columbia University, New York, NY 10027, USA. [3]Department of Materials Science and Chemical Engineering, Stony Brook University, Stony Brook, NY 11794, USA. [4]Department of Chemical Engineering, Columbia University, 817 SW Mudd, New York, NY 10027, USA. [5]National Synchrotron Light Source II, Brookhaven National Laboratory, Upton, NY 11973, USA.
*Corresponding author. Email: og2226@columbia.edu (O.G.); cynam@bnl.gov (C.-Y.N.)

functional organic-inorganic hybrids and creating inorganic nanostructures (*33*–*40*). They have proven useful not only in improving polymer properties, such as etch resistance, rheological and mechanical responses, and optical properties (*41*–*47*), but also in the patterning of electronic devices (*35*, *37*, *46*, *48*–*50*). The infiltration techniques have also been shown valuable for creating a library of metals and metal oxides within polymeric structures (*35*, *51*–*58*). Given the structural designability of DNA-based nanomaterials, it would be advantageous to use infiltration-driven hybridization processes to 3D DNA structures to convert them into organic-inorganic hybrids and inorganic nanoreplicas (*59*).

Here, we demonstrate the application of LPI and VPI for inorganic templating of large-scale DNA frameworks. The 3D templating, thus realized, allows us to achieve deep penetration into 3D nanoarchitectures and to apply these methods, separately or together, to form different functional metal and metal oxide frameworks based on the designed DNA scaffold frameworks. Sol-gel growth of silica followed by the infiltration synthesis provides versatile and modular control over the spatial distribution and elemental composition of inorganic material incorporated into a framework superlattice. The incorporation of single-element and multielement coatings by exploiting LPI or VPI techniques, or their combination, preserves the underlying DNA lattice architecture while enabling a nanofabrication of 3D inorganic nanoscale frameworks.

RESULTS AND DISCUSSION

The formation of the DNA superlattice frameworks starts with synthesizing the DNA origami precursors. Briefly, DNA origami frames are formed from the folding of a long scaffold strand of M13 phage DNA with many short synthetic strands of complementary DNA. Here, we synthesize both octahedral (edge length, ~29 nm) and tetrahedral (edge length, ~36 nm) motifs for the self-assembly of superlattices (*60*). Following synthesis of the origami precursor, the DNA frames with complementary binding strands, placed at their vertices, were mixed together and annealed from 50°C to room temperature at a rate of −0.2°C/hour to form 3D DNA frameworks. Sol-gel wet chemistry was used to grow a 4- to 10-nm-thick layer of silica on the DNA bundles of each type of framework (see Fig. 1A and the Supplementary Materials) (*24*, *61*), thus forming silica replica of the DNA framework. The two different motifs result in two pore sizes, ~50 to 60 nm for tetrahedron and 10 to 20 nm for octahedral assembles. For most work described, the octahedral motif is used; in select cases, both tetrahedral and octahedral motifs were experimented to gauge the generality of the approach (see the Supplementary Materials for further information).

Active sites with —OH groups in the formed silica network of DNA-prescribed framework replica can be directly coupled with the application of VPI (Fig. 1B) and LPI (Fig. 1C) for inorganic templating. In these processes, vapor- or liquid-phase precursors are attracted and bound to the surface —Si or —OH group (*32*, *35*), yielding precise surface coating of target materials on the silica framework (see figs. S1 and S2). Furthermore, the pore structure of the frameworks (pore size, ~10 to 20 nm) lends itself well to applying LPI and VPI by allowing unhindered transport of precursors into the interior of the silica origami framework. The resultant nanostructure has conformal coatings of metals infiltrated via VPI and/or LPI techniques shown in Fig. 1 (D and E), demonstrating the metal coating onto the interior pore surfaces within the silica/DNA nanostructure.

First, we investigated the use of LPI, where the silicated DNA nanostructures situated on a Si substrate were exposed to a drop-cast solution of a metal salt of interest [dispersed in water or ethanol (EtOH)]. Silica frameworks were incubated for 5 min to enable the sorption of metal ions to the silica superlattice, as shown in Fig. 2A. After removing the solution by spin-drying,

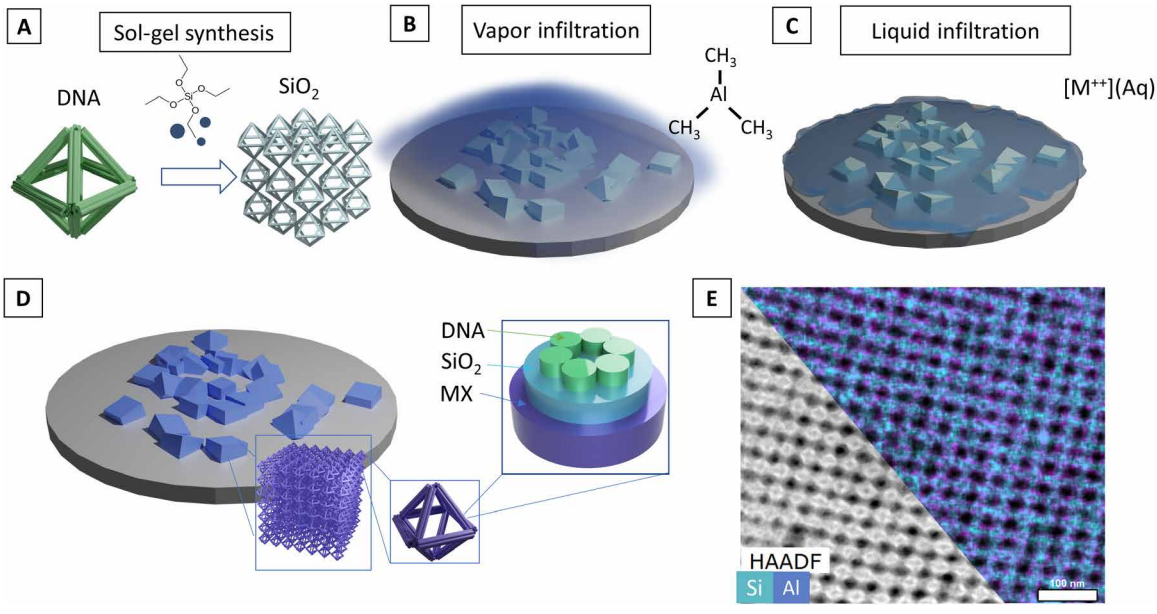

Fig. 1. Inorganic templated structures. (**A**) A silica 3D framework is formed when a lattice of DNA frames is coated with a layer of silica grown via sol-gel synthesis. Templating of the framework is achieved either by (**B**) VPI, where a vapor precursor such as TMA infiltrates the silica framework, or (**C**) LPI, whereby metal salt solutions infiltrate the nanolattice structure. (**D**) The resultant nanolattice after heat treatment is composed of conformal coatings of silica and metal/metal oxide (MX) on a DNA scaffold. (**E**) Scanning TEM (STEM) cross-sectional HAADF imaging and EDS map of silica (blue) coated with alumina (purple) via vapor infiltration. Scale bar, 100 nm.

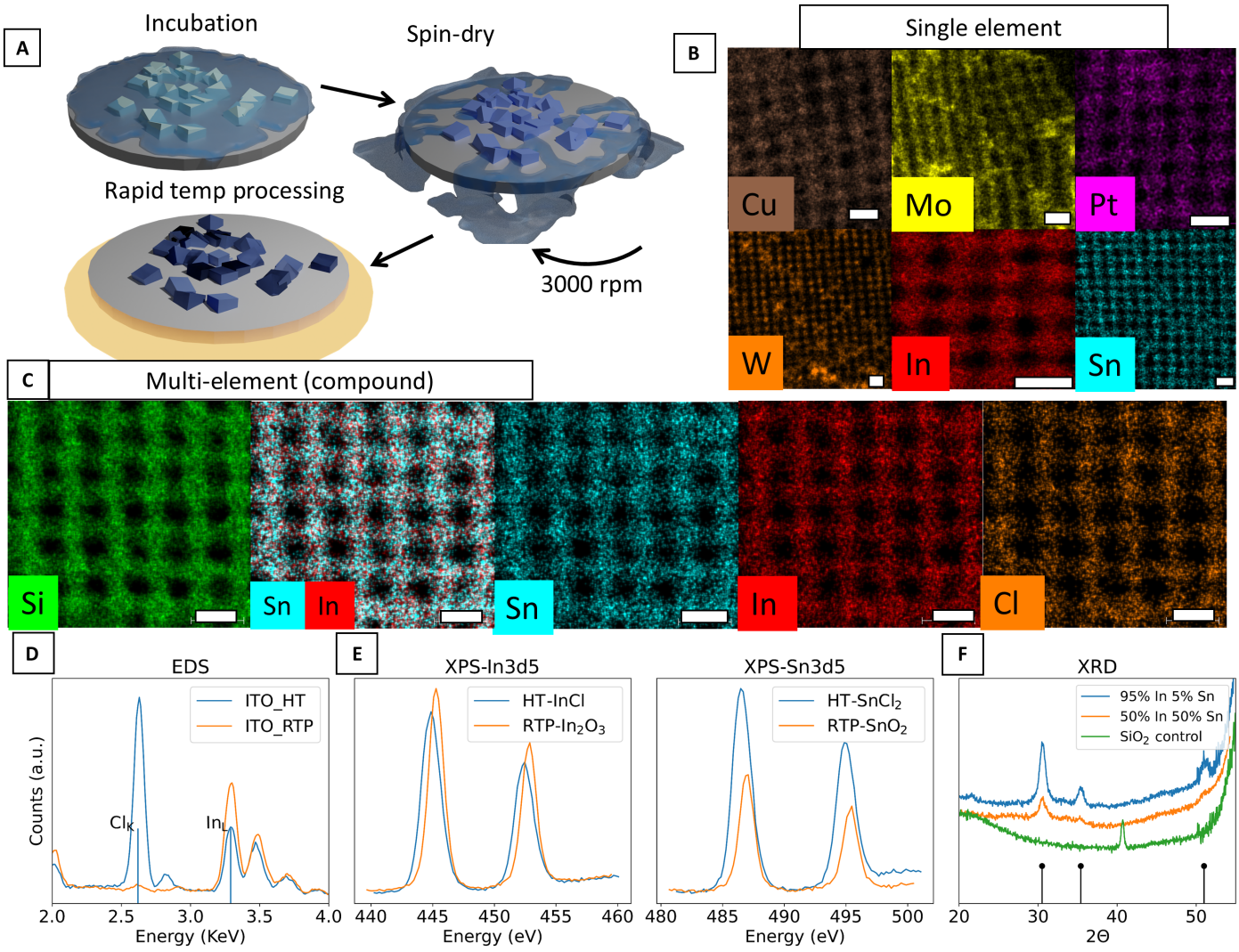

Fig. 2. LPI. (**A**) Schematic of LPI process—after drop-casting of specific concentration of the metal salt solution, silica superlattice is incubated for a variable amount of time, leading to adsorption and deposition of the metal ions on the framework. This was followed by spin-drying and thermal annealing. (**B**) TEM cross-sectional images of single-element liquid–infiltrated silica superlattices coated with specific elements such as copper, molybdenum, platinum, tungsten, indium, and tin. Scale bars, 50 nm. (**C**) Multielement incorporation of indium and tin, with the silicon, followed by combined elemental map of indium, and tin, and individual elemental maps of tin, indium, and chlorine. Scale bars, 50 nm. (**D**) EDS of chlorine signal before (blue) and after (orange) RTP in oxygen at 600°C. (**E**) XPS spectra of the binding energy shift of In and Sn 3d5 peaks before (blue) and after (orange) RTP in oxygen. (**F**) X-ray diffraction spectra after RTP of 50:50 (orange) and 95:5 (blue) indium:tin composition compounds along with a control silica nanolattice. Crystalline peaks for ITO are shown with black markers. a.u., arbitrary units.

the metal-incorporated nanostructures are then thermally annealed in a tube furnace in air at 250°C for 5 min to remove water/EtOH. To arrive at optimal conditions for liquid-phase growth, metal salt concentration was held constant at 20 mM, and incubation time was varied. Sodium tetrachloroplatinate was selected as the template platinum salt solution due to its long shelf life (~4 to 6 months) to investigate templating parameters. We then applied energy-dispersive spectroscopy (EDS) characterization for samples incubated with sodium tetrachloroplatinate for 1 to 20 min to study the templating process. EDS measurements showed that atomic percentage plateaued for incubation time above 10 min (see fig. S3). Further investigation with transmission electron microscopy (TEM) demonstrated that nanostructures were self-limiting and that further incubation did not result in the growth of a thicker coating. On the other hand, TEM cross section of the 2-min versus 5-min incubation (see fig. S4) demonstrated that 2 min did not allow for homogeneous growth due to insufficient penetration into the lattice framework, whereas 5 min provided an even distribution of metal throughout. For all subsequent metal species demonstrated in this work, the precursor solution concentration (20 mM) and incubation time were kept constant at 5 min for comparison.

For incorporating a single-element species, both simple and complex chloride salts coordinated by ammonium or sodium were investigated, including indium chloride, ammonium tetrachlorocuprate dihydrate, ammonium molybdate tetrahydrate, ammonium tungstate, ammonium tin chloride, sodium tetrachloroaurate, and sodium tetrachloroplatinate. In Fig. 2B, we show the TEM-obtained cross-sectional elemental mapping data based on EDS measurements of templated

frameworks for various elements, including copper, molybdenum, platinum, tungsten, indium, and tin. The formed inorganic frameworks consist of 4- to 5-nm thickness of these materials coated onto the surface of silica frameworks and with high spatial fidelity, as defined by 3D DNA-assembled scaffold (see figs. S5 to S11).

The simultaneous incorporation of multiple elements into a single nanocomposite framework lattice was further demonstrated by combining indium and tin for a multielement superlattice composite. The cross-sectional TEM imaging (Fig. 2C and fig. S12) identifies nanocoated indium and tin along with chlorine, from the complex anion of the chloride salt–based precursor solutions. Heat treatment at 300°C in air with a 50:50 molar composition of indium and tin salt precursor oxidizes the metals to a limited extent but causes the removal of tin as measured by x-ray photoemission spectroscopy (XPS) (fig. S13). Applying a rapid temperature processing (RTP) in oxygen at 600°C for 5 min effectively preserves the intended metal composition and removes chlorine from the framework. This was confirmed by scanning electron microscopy (SEM) with EDS (Fig. 2D), applied on the infiltrated superlattice, which probes the elemental makeup of the sample volumetrically. The rapid thermal treatment oxidizes the structure to indium tin oxide (ITO), as shown in the XPS spectra collected before and after the RTP (Fig. 2E). The observed shifts of the indium and tin binding energies upon RTP compared with those in their respective tin and indium chloride states agree with what is expected from oxidation (see fig. S14) (*62*). X-ray diffraction data, performed on two motifs of ITO composites, 95%:5% and 50%:50% (In:Sn) Fig. 2F, along with XPS measurements support the formation of crystalline ITO on the silica superlattice framework. Further characterization by high-resolution TEM revealed crystalline domains of the order of 7 nm (fig. S15).

Next, we explored templating silica frameworks using VPI (*63*–*67*), derived from atomic layer deposition (ALD). The silica replicas of DNA lattices were exposed to vapor-phase organometallic precursors, such as trimethylaluminum (TMA) and diethylzinc (DEZ) for AlO_x and ZnO_x, respectively, and water (oxidant) in a cyclic manner using the microdose precursor exposure protocol (*35*, *68*), as shown in Fig. 3A. During the normal ALD process, carrier gas such as N_2 or Ar flows continuously, and material precursors, such as TMA and H_2O for AlO_x, are briefly pulsed (for tens of milliseconds) sequentially, with each pulse being separated by a short waiting period (a few seconds) to complete one ALD cycle. The constant purging and evacuation during normal ALD in principle ensure that unreacted precursors are removed from the surface and only monolayer deposition occurs per ALD cycle. However, for large 3D structures with

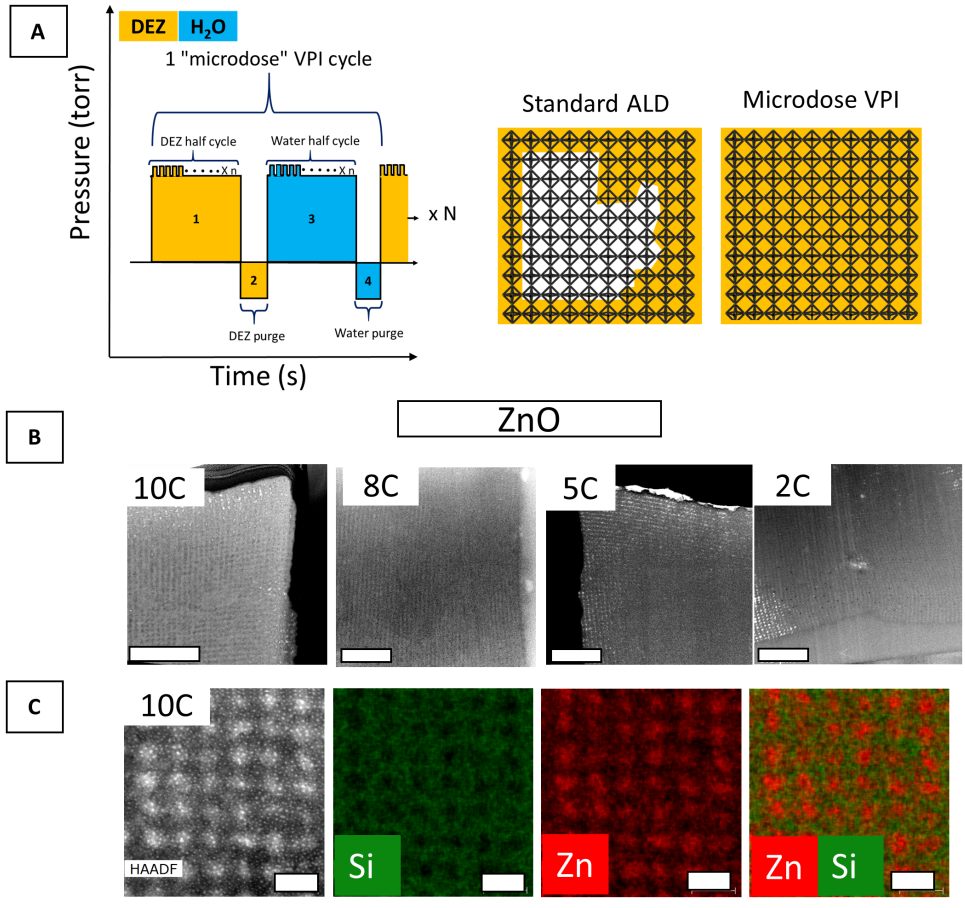

Fig. 3. VPI. (**A**) Microdosing VPI cycles on a silica superlattice producing nanotemplated metal/oxides frameworks. Comparing conformal VPI coating with standard ALD that can induce a spurious growth of the precursor. (**B**) Cross-sectional TEM of zinc oxide–infiltrated nanolattices with cycles (2C to 10C, with "C" denoting cycle). At 2C, pores (white) can still be seen in the nanostructure reaching into the center of the structure; at 5C, the edges are still mostly empty; at 8C and 10C, the structure is filled with ZnO as seen from the dark regions filling pores. Scale bars, 500 nm. (**C**) STEM-HAADF EDS of the 10C superlattice showing the bright area to be rich in Zn and the dark areas to be rich in Si. Scale bars, 50 nm.

small, sub–50-nm pores like the DNA-derived nanolattice, such a normal ALD protocol does not allow enough time for precursors to fully penetrate into the interior section of the 3D porous structure or for unreacted precursors to fully diffuse out of the interior, therefore leading to a clogged material deposition limited to subsurface depth of a nanolattice, as schematically shown in Fig. 3A and fig. S16.

In contrast, during VPI process, the precursor pulsing cycles are initiated under a static vacuum (i.e., no carrier gas flow, with the reactor chamber being isolated from evacuation), followed by a long "exposure period" (up to tens of minutes or even hours) before reevacuating and purging the chamber; this exposure period allows the precursors to fully diffuse (i.e., infiltrate) into a large, 3D porous nanostructure and get deposited within the pore interior surfaces. Specifically for this study, material precursors were exposed to the silica nanolattice under a static vacuum for 600 s, followed by purging with flowing nitrogen and evacuation for the same duration. Again, the long exposure ensured enough time for the precursors to fully diffuse into the entire porous silicated DNA lattice and bind to reactive surface sites on the frame struts of the nanostructure. At the same time, the long purge removed most of the excess precursor physiosorbed and/or kinetically trapped within the pore, preventing uncontrolled spurious deposition and associated pore clogging. The infiltration approach thus preserved the nanostructure architecture. However, it is noted that given the large size of superlattice (in approximately micrometers) domains, some of these extra precursors still remain inside, contributing to the deposition of material amounts beyond the normal ALD limit during the VPI process. This effect becomes evident for a 3D structure with smaller nanopores—if silica growth resulted in pores less than 10 nm, then nanolattices showed similar clogging to standard ALD (see fig. S17). Thus, following VPI coating, we then probed the internal penetration of vapor-phase precursors and the resulting 3D inorganic templating into the silicate lattice framework using cross-sectional TEM analysis.

The cross section of the ZnO_x-infiltrated silicate superlattice (Fig. 3B and fig. S18) displayed a complete filling of the pores of the internal structure after 10 VPI cycles. Reducing the number of VPI cycles from 10 to 2 decreases the total amount of infiltrated ZnO_x into the structure, while not substantially cutting down on overgrowth (see fig. S19 for additional cross-sectional imaging). High-angle annular dark-field (HAADF) imaging of the 10-cycle structure (Fig. 3C) shows the silica as a network lattice (black) with white areas representing ZnO_x, as revealed by EDS elemental maps of the region.

Applying a 10-cycle AlO_x VPI using TMA precursor resulted in a 5- to 7-nm growth of AlO_x on the strut surface, leaving open pores in the framework rather than completely filling the pore as in the ZnO_x case. The AlO_x infiltration appeared uniform across the 5-μm-wide superlattice sample, as shown in Fig. 4A and figs. S20 and S21. The difference in the apparent growth rate between the TMA and DEZ growth on the silica superlattice is attributed to subtle differences in the organometallic precursor affinities for the —OH bonds on the surface of the silica framework.

Leveraging the uniform coating of AlO_x on the silica framework struts, a single cycle of AlO_x VPI was used as an initial passivating step (AlO_x priming) before ZnO_x VPI for the controlled growth of ZnO_x layer. AlO_x priming and 6 ZnO_x VPI cycles resulted in a uniform coating on the superlattice with pores extending throughout the structure. In Fig. 4B, we show that we can tune the amount of Al versus Zn in the superlattice while retaining the nanostructure. As the number of AlO_x priming cycles is increased relative to ZnO_x VPI cycles, the relative amount of alumina increased as seen in accompanying HAADF-EDS maps of samples with increasing Al cycles. The EDS qualitatively showed that increasing TMA from 1 to 3 cycles increased the atomic % from 10 to >30 of the matrix makeup, while the signal for zinc stayed approximately the same comparing 4, 5, and 6 cycles (see Fig. 4B and figs. S22 to S25).

We further investigated the electrical conductivity and optoelectronic properties of the resulting aluminum-doped ZnO (AZO) framework, as shown in Fig. 4C. Pt electrical contacts were patterned to connect to an isolated nanolattice. We observed four orders of magnitude increase in the measured current for AZO nanolattice compared to the nominal silica nanolattice.

The photoluminescence (PL) spectroscopy measurements (Fig. 4D) on the zinc oxide superlattice demonstrated characteristic near band edge emission in the ultraviolet (UV) region at ~375 nm and a broad emission from 380 to 500 nm (*69*, *70*). The broad emission is related to atomic impurities and defect emission and dopants from the underlying silica. This broad defect emission region is further enhanced upon the addition of aluminum priming to the VPI, analogous to common approaches to enhancing the green emission of ZnO devices (*71*).

Having demonstrated the capability to coat the structure with multiple individual elements and their combinations, we further demonstrate combining LPI and VPI methods to broaden the possible material composition of frameworks. As a case example, we combined platinum LPI alongside aluminum-primed zinc oxide VPI by successive processing and characterized the resulting structures by cross-sectional electron microscopy. The optimal coating was found by performing VPI of alumina-primed zinc oxide, followed by LPI of platinum (see figs. S26 and S27 for LPI followed by VPI). A schematic of the system is shown in Fig. 5A, whereby the DNA followed by silica coating is layered with alumina-primed zinc oxide and platinum, as imaged by SEM. Cross-sectional EDS maps (Fig. 5B) show uniform internal coatings of all three elements on the silica nanostructure. Further high-resolution TEM reveals crystalline domains within 5- to 10-nm coating (Fig. 5, C and D, inset).

The global structure from selected area diffraction shows polycrystalline domains of ZnO and platinum throughout the Pt-AZO-silica framework structure (see fig. S28). Simultaneous small-angle and wide-angle x-ray scattering (SAXS/WAXS) of the formed structure (Fig. 5E) reveals nanoscale and atomic structure of frameworks. Scattering captures their hierarchical organization with an SAXS peak at 0.0148 $Å^{-1}$ corresponding to the 42-nm spacing simple cubic nanolattice of DNA octahedra frames, while on atomic scale, zinc oxide and platinum oxide are in hexagonal $P6_3mc$ and in $Fm\bar{3}m$ space groups, respectively. To further probe the 3D structure volumetrically and determine whether the architecture and elemental composition are consistent throughout the entire Pt-AZO-silica framework domains, we performed scanning hard x-ray microscopy. By leveraging the fluorescence from platinum and zinc when excited by the 12-keV photon beam, 3D tomographic data were collected at the hard x-ray nanoprobe (HXN) beamline of National Synchrotron Light Source II. The x-ray phase image at each projection angle was retrieved from far-field diffraction patterns with ptychography algorithm (*72*), aligned, and stacked with simultaneous fluorescence (see figs. S29 to S31) (*61*). They are then used for tomographic reconstruction (*61*, *73*) of formed frameworks. The reconstructed 3D framework volume depicts the correspondence between the spatial features of the phase image, which reflects the electron density variations, and both reconstructed platinum and zinc fluorescence

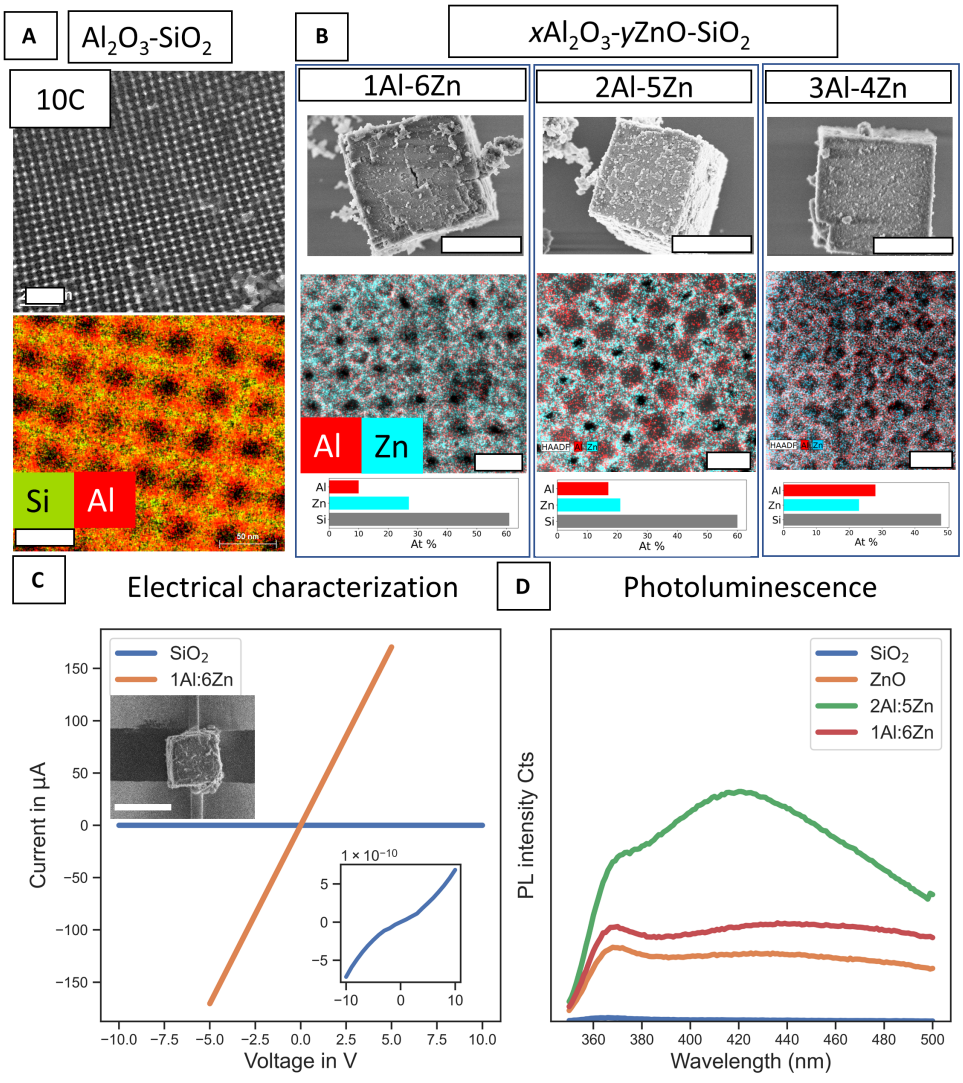

Fig. 4. Fabrication and characterization of AZO frameworks. (**A**) TEM and EDS map of 10-cycle VPI of alumina. Scale bars, 200 and 50 nm. (**B**) Mixed TMA cycles and DEZ cycles (cycles alumina:cycles zinc) for three conditions 1:6, 2:5, 3:4, where EDS is used to show the relative amount of alumina versus zinc (Al in red and Zn in cyan). Scale bars, 3 µm (SEM) and 50 nm (HAADF). At %, atomic %. (**C**) Demonstration of the increased electrical conductivity of the AZO framework compared to the base silica framework by means of an *I-V* curve along with inset of control silica. Scale bar, 5 um. (**D**) PL spectra of studied silica, ZnO-silica, and Al-ZnO-silica (1:6 and 2:5 Al:Zn) frameworks.

maps, as shown in Fig. 5 (F and G). The central slice through the volume (see Fig. 5H and movies S1 and S2) further corroborates the 3D templating of the platinum and zinc on silica framework, thus demonstrating a successful formation of 3D Pt-AZO-silica frameworks.

In conclusion, here, we have demonstrated that designed superlattices of DNA frames can be used as scaffolds for the fabrication of single-element and composite inorganic frameworks with prescribed 3D architecture. Given a large library of metal salts and ALD precursors suitable for deposition on silica, the liquid and vapor infiltration protocols allow for the fabrication of diverse inorganic nanostructures through templating DNA-prescribed nanolattice frameworks. We have established 3D templating approaches and investigated the chemical and structural states of these inorganic frameworks. The study demonstrates the development of LPI and VPI after processing to fully oxidize infiltrated metals within frameworks. The electrical and optical properties of semiconductor frameworks were explored. The possibility to transfer a multitude of DNA-defined geometries to a large structural diversity of inorganic materials opens possibilities for generating open framework 3D nanostructures with optical, mechanical, electrical, and catalytic functions. Thus, the presented 3D nanofabrication strategy might be vital for enabling a broad range of application requiring 3D nanostructures with complexly prescribed architectures and compositions. The work paves a road for establishing 3D lithography methods based on molecularly programmed architectures.

MATERIALS AND METHODS

DNA origami synthesis and superlattice assembly

DNA-origami octahedra were formed by mixing M13mp18 DNA scaffold and DNA staples strands with a 1:5 ratio in 1× TAE buffer (40 mM tris acetate and 1 mM EDTA) with 12.5 mM Mg^{2+} and

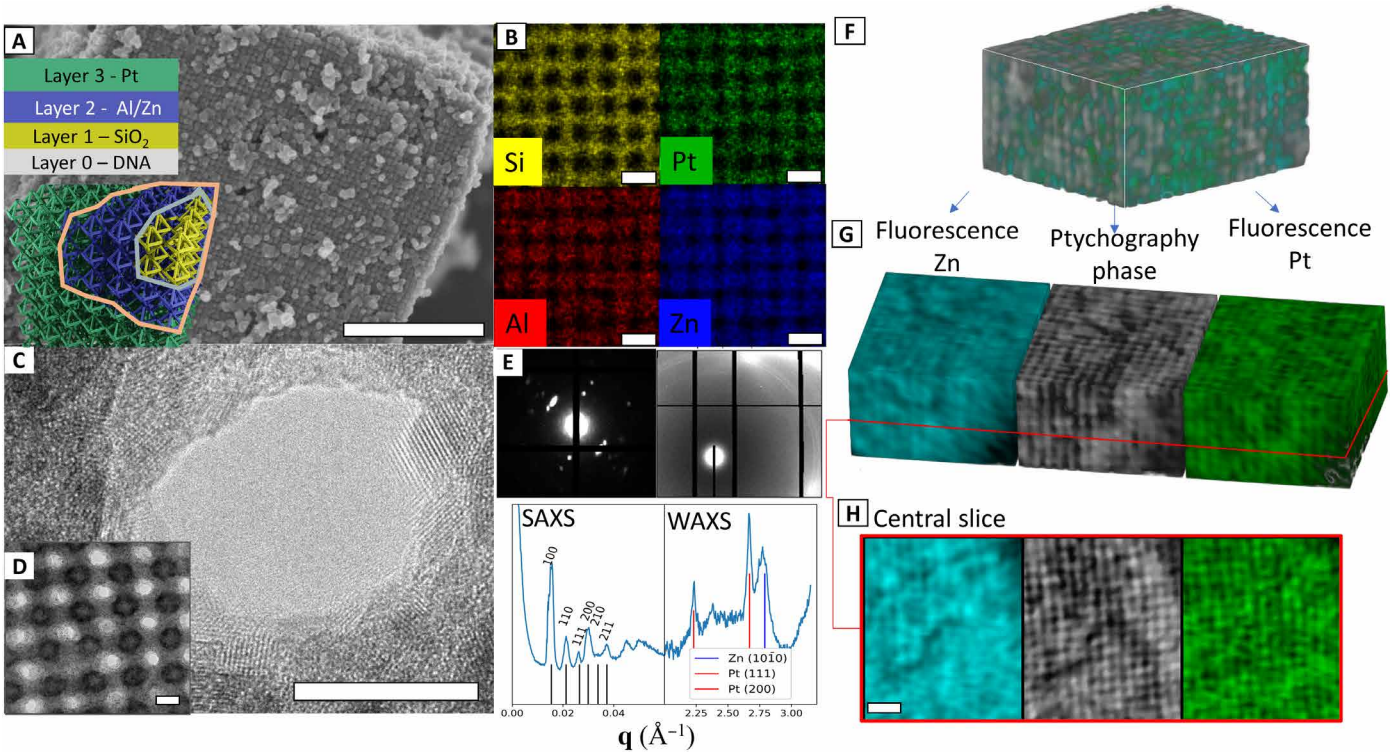

Fig. 5. Composite frameworks via combined VPI and LPI. (**A**) SEM micrograph of VPI/LPI nanostructure of platinum on alumina doped zinc oxide. Scale bar, 1 μm. (**B**) Cross-sectional EDS maps of the structure with channels for platinum, silicon, alumina, and zinc. Scale bars, 50 nm. (**C**) High-resolution TEM of pore within framework showing crystalline domains of platinum encircling the interior of the structure along the strut walls. Scale bar, 10 nm. (**D**) Zoomed out region from (C), white represents holes in the structure, and black is the nanolattice. Scale bar, 20 nm. (**E**) 2D SAXS (left) and WAXS (right) patterns of frameworks deposited on a silicon wafer with corresponding 1D reduction plotting scattering intensity versus wave vector **q**. Nanoscale (simple cubic) and atomic indexing of diffractions planes are shown. (**F**) Scanning x-ray nanotomography of a Pt-AZO superlattice combined phase and fluorescence reconstructions. (**G**) Separate volumetric views of the reconstructed phase and fluorescence (zinc and platinum) of a framework. (**H**) A 2D slice from the central 3D volume of the reconstruction. Scale bar, 100 nm.

slowly annealed over 20 hours from 90°C to room temperature over the course of 20 hours for origami formation, overall a ramp rate of −0.2°C/hour. Superlattices of DNA origami was formed by mixing DNA-origami octahedra with complementary DNA bases at the vertices. The origami were mixed to form a 20 nM concentration solution at 20 to 50 μl. The sample was annealed in a polymerase chain reaction over 5 days from 50°C to room temperature at −0.2°C/hour. Robust DNA origami superlattices were made by growing a layer of silica on the DNA bundle. For conversion to inorganic silica, superlattices were centrifuged, and supernatant was replaced with 0.1× TAE with 10 mM Mg. Separately silication buffer was prepared by adding 2.5 μl of (3-aminopropyl)-triethoxysilane and 10 μl of tetraethoxysilane in a 0.1× TAE with 10 mM Mg buffer for a total volume of 500 μl. The solution was vortexed at 700 rpm for 30 min, filtered with a 0.2-μm Millex-GV polyvinylidene difluoride filter to remove large particulates, and then 5 μl of superlattice and 10 μl of the filtered silication buffer are mixed together. The solution was vortexed at 700 rpm for 1 to 2 hours and then centrifuged, and the buffer was exchanged with water.

Structural and elemental characterization

Superlattices were characterized using SEM (Hitachi S-4800), analytical SEM (Jeol 7600F SEM-EDS), and scanning TEM (FEI Talos F200X; 200 kV; equipped with the EDS elemental mapping capability). The cross-sectional TEM samples were prepared by the standard in situ lift-out procedure using Ga ion milling in a focused ion beam system (FEI Helios 600 Nanolab). X-ray diffraction was performed on a Rigaku Smartlab operating in 1D grazing incidence using a zero diffraction silicon substrate. XPS was collected on a PHI Versaprobe II at CUNY Advanced Science Research Center.

Scanning hard x-ray tomography

The experiment was conducted at the 3-ID HXN beamline of the National Synchrotron Light Source II, Brookhaven National Laboratory. Superlattices coated in platinum-aluminum–primed zinc oxide–silica superlattice were prepared with in situ lift-out procedure using Ga ion milling to fashion a ~1-μm domain on a tungsten pin.

A monochromatic beam at 12 keV was selected and focused by multilayer Laue lenses to a nanobeam of ~13 nm. Flyscans were carried out in a grid of 120 × 100 with a step size of 10 nm with a 30-ms dwell time. In total, 135 projections were used for reconstruction representing angles from −90 to +44. Far-field diffraction was collected downstream, while fluorescence was collected from an energy-dispersive detector placed 90° from the beam to collect x-rays. Elements were fitted by PyXRF software package; separately, ptychography was performed on the far-field diffraction and recover the complex value probe and object function. The probe was subsequently used with state-of-the-art deconvolution techniques to further refine the simultaneously collected fluorescence.

Small-angle x-ray scattering/wide-angle x-ray scattering

Scattering experiments were performed at the small matter interfaces (12-ID) beamlines of the National Synchrotron Light Source II, Brookhaven National Laboratory. A 16.1-keV beam was microfocused beam (2 × 25 μm) using compound refractive lens transfocator and was brought to the sample in transmission with a SAXS detector, Pilatus 1M, 8.3 m away, and simultaneous WAXS detector Pilatus 900KW 0.275 m from the sample. SAXS and WAXS results were reduced to 1D and fitted with GitHub-CFN-softbio/SciAnalysis: SciAnalysis is a set of Python scripts for batch processing of image data, including x-ray scattering detector images (https://github.com/CFN-softbio/SciAnalysis); and GitHub-CFN-softbio/ScatterSim: Mesoscale SAXS powder simulations (https://github.com/CFN-softbio/ScatterSim).

Normal ALD coating of TiO_x and AlO_x on DNA lattices

The DNA lattices were coated with TiO_x and AlO_x thin film using Cambridge Nanotech Savannah S100 ALD system (base pressure, ~0.35 torr) at 85°C. During each TiO_x ALD cycle, titanium (IV) isopropoxide and water vapor were alternatively pulsed each for 0.4 s with 5-s interval under continuous N_2 flow. Each AlO_x ALD includes 15-ms pulsation of TMA and water vapor pulsing, separated by a 10-s N_2 purging. In total, 50 cycles were used to deposit TiO_x and 10 cycles for AlO_x.

Vapor-phase infiltration

The infiltration of ZnO, Sn, and AlO_x on the silicate superlattices was carried out in a commercial ALD system (Cambridge Nanotech, Savannah S100) at 85°C using DEZ and TMA as respective metal organic precursors along with water as an oxidant. A single ZnO infiltration cycle by the microdose protocol consists of the following, in sequence: exposure to DEZ for 600 s under a static vacuum (~1.7 torr), chamber purging using N_2 [100 standard cubic centimeters per minute (sccm)] for 600 s, exposure to water vapor for 600 s, and chamber purging using N_2 (100 sccm) for 600 s. A single AlO_x infiltration cycle by the microdose protocol consists of the identical steps described above (chamber pressure of ~1000 torr during TMA infiltration). During the microdose precursor exposure period of 600 s, the precursor (both DEZ/TMA and water) dosing was repeated every 60 s during the exposure period (a total of 10 repeated dosings). The infiltration was followed by the initial removal of the organic polymer matrix by oxygen plasma ashing (20 W, 100 mtorr, 5 min, room temperature) and the further consolidation of the inorganic matrix and the removal of carbon impurities by O_2 RTP treatment at 600°C for 5 min (Modular Process Technology, RTP-600S).

Liquid-phase infiltration

Infiltration of metal salts diluted in either EtOH or deionized water was spin-coated onto superlattices dispersed on a silicon substrate. Nominally, 20 μl of a 20 mM metal salt solution was deposited on the sample for 5 min, followed by spin-drying at 3000 rpm for 30 s. This was either followed by RTP or 5 min in a tube furnace in the air set to 250°C.

Electrical testing

The two-probe current-voltage relation (*I-V*) characteristics of devices were measured using an electrical probe station (Signatone) equipped with a dark box and a high-precision semiconductor parameter analyzer (Agilent). For the illuminated (*I-V*) characteristics, the devices were soaked for 2 min under the microscope's tungsten light before initiating measurements.

Chemicals

Metal salts were purchased from Sigma-Aldrich and Alfa Aesar. All chemicals were diluted to 20 mM in either water or EtOH. Approximately 20 μl was dropped onto the surface of silicon substrate with silica-coated DNA superlattice spread on the surface for 5 min. The samples were then spun at 3000 rpm for 30 s, followed by thermal annealing in air at 250°C or RTP at 600°C in oxygen. For combinations, equal volumes were mixed and drop-cast onto the superlattices. The following chemicals were attempted, and supplemental figures will indicate the specific metal salt for duplicate chemistries: platinum (Na_2PtCl_4 in water), gold ($NaAuCl_4$ in water or EtOH), tin (H_4SnCl_6 in EtOH), copper (NH_4CuCl_4 in EtOH), molybdenum [$(NH_4)_6Mo_7O_{24}$ in water], tungsten [$(NH_4)_6H_2W_{12}O_{40}$ in water], and indium ($InCl_3$ in EtOH).

Supplementary Materials

This PDF file includes:

Figs. S1 to S31

Legends for movies S1 and S2

Other Supplementary Material for this manuscript includes the following:

Movies S1 and S2

REFERENCES AND NOTES

1. J. A. Liddle, G. M. Gallatin, Nanomanufacturing: A perspective. *ACS Nano* **10**, 2995–3014 (2016).
2. T. Tanaka, A. Ishikawa, Towards three-dimensional optical metamaterials. *Nano Converg.* **4**, 34 (2017).
3. A. Michelson, T. J. Flanagan, S.-W. Lee, O. Gang, High-strength, lightweight nano-architected silica. *Cell Rep. Phys. Sci.* **4**, 101475 (2023).
4. L. Gloag, A. R. Poerwoprajitno, S. Cheong, Z. R. Ramadhan, T. Adschiri, J. J. Gooding, R. D. Tilley, Synthesis of hierarchical metal nanostructures with high electrocatalytic surface areas. *Sci. Adv.* **9**, eadf6075 (2023).
5. M. A. Saccone, R. A. Gallivan, K. Narita, D. W. Yee, J. R. Greer, Additive manufacturing of micro-architected metals via hydrogel infusion. *Nature* **612**, 685–690 (2022).
6. J. Li, J. Yan, L. Jiang, J. Yu, H. Guo, L. Qu, Nanoscale multi-beam lithography of photonic crystals with ultrafast laser. *Light: Sci. Appli.* **12**, 164 (2023).
7. Y. Liang, M. Frederik, H. F. B. Uwe, B. Eva, W. Martin, Multi-material multi-photon 3D laser micro- and nanoprinting. *Light: Adv. Manuf.* **2**, 296–312 (2021).
8. Z. C. Ma, Y. L. Zhang, B. Han, Q. D. Chen, H. B. Sun, Femtosecond-laser direct writing of metallic micro/nanostructures: From fabrication strategies to future applications. *Small Methods* **2**, 1700413 (2018).
9. K. W. Tan, U. Wiesner, Block copolymer self-assembly directed hierarchically structured materials from nonequilibrium transient laser heating. *Macromolecules* **52**, 395–409 (2019).
10. A. Klinkova, R. M. Choueiri, E. Kumacheva, Self-assembled plasmonic nanostructures. *Chem. Soc. Rev.* **43**, 3976–3991 (2014).
11. C. Yuan, W. Ji, R. Xing, J. Li, E. Gazit, X. Yan, Hierarchically oriented organization in supramolecular peptide crystals. *Nat. Rev. Chem.* **3**, 567–588 (2019).
12. M. A. Boles, M. Engel, D. V. Talapin, Self-assembly of colloidal nanocrystals: From intricate structures to functional materials. *Chem. Rev.* **116**, 11220–11289 (2016).
13. Y. Li, W. Zhou, I. Tanriover, W. Hadibrata, B. E. Partridge, H. Lin, X. Hu, B. Lee, J. Liu, V. P. Dravid, K. Aydin, C. A. Mirkin, Open-channel metal particle superlattices. *Nature* **611**, 695–701 (2022).
14. S.-H. Yu, R. O'Reilly, L. Jiang, N. A. Kotov, The new era of self-assembled nanomaterials. *Acc. Chem. Res.* **55**, 1783–1784 (2022).
15. J. S. Kahn, O. Gang, Designer nanomaterials through programmable assembly. *Angew. Chem. Int. Ed.* **61**, e202105678 (2022).
16. F. Hong, F. Zhang, Y. Liu, H. Yan, DNA origami: Scaffolds for creating higher order structures. *Chem. Rev.* **117**, 12584–12640 (2017).
17. T. Zhang, C. Hartl, K. Frank, A. Heuer-Jungemann, S. Fischer, P. C. Nickels, B. Nickel, T. Liedl, 3D DNA origami crystals. *Adv. Mater.* **30**, e1800273 (2018).
18. P. W. Rothemund, Folding DNA to create nanoscale shapes and patterns. *Nature* **440**, 297–302 (2006).
19. S. M. Douglas, H. Dietz, T. Liedl, B. Högberg, F. Graf, W. M. Shih, Self-assembly of DNA into nanoscale three-dimensional shapes. *Nature* **459**, 414–418 (2009).
20. L. Shani, P. Tinnefeld, Y. Fleger, A. Sharoni, B. Y. Shapiro, A. Shaulov, O. Gang, Y. Yeshurun, DNA origami based superconducting nanowires. *AIP Adv.* **11**, 015130 (2021).

21. Y. Geng, J. Liu, E. Pound, S. Gyawali, J. N. Harb, A. T. Woolley, Rapid metallization of lambda DNA and DNA origami using a Pd seeding method. *J. Mater. Chem.* **21**, 12126–12131 (2011).
22. A. C. Pearson, J. Liu, E. Pound, B. Uprety, A. T. Woolley, R. C. Davis, J. N. Harb, DNA origami metallized site specifically to form electrically conductive nanowires. *J. Phys. Chem. B.* **116**, 10551–10560 (2012).
23. R. Wang, G. Zhang, H. Liu, DNA-templated nanofabrication. *Curr. Opin. Colloid Interface Sci.* **38**, 88–99 (2018).
24. P. W. Majewski, A. Michelson, M. A. L. Cordeiro, C. Tian, C. Ma, K. Kisslinger, Y. Tian, W. Liu, E. A. Stach, K. G. Yager, O. Gang, Resilient three-dimensional ordered architectures assembled from nanoparticles by DNA. *Sci. Adv.* **7**, eabf0617 (2021).
25. Y. Shang, N. Li, S. Liu, L. Wang, Z. G. Wang, Z. Zhang, B. Ding, Site-specific synthesis of silica nanostructures on DNA origami templates. *Adv. Mater.* **32**, e2000294 (2020).
26. X. Liu, F. Zhang, X. Jing, M. Pan, P. Liu, W. Li, B. Zhu, J. Li, H. Chen, L. Wang, Complex silica composite nanomaterials templated with DNA origami. *Nature* **559**, 593–598 (2018).
27. L. Nguyen, M. Döblinger, T. Liedl, A. Heuer-Jungemann, DNA-origami-templated silica growth by sol-gel chemistry. *Angew. Chem. Int. Ed.* **58**, 912–916 (2019).
28. M.-K. Nguyen, V. H. Nguyen, A. K. Natarajan, Y. Huang, J. Ryssy, B. Shen, A. Kuzyk, Ultrathin silica coating of DNA origami nanostructures. *Chem. Mater.* **32**, 6657–6665 (2020).
29. S. Wu, M. Zhang, J. Song, S. Weber, X. Liu, C. Fan, Y. Wu, Fine customization of calcium phosphate nanostructures with site-specific modification by DNA templated mineralization. *ACS Nano* **15**, 1555–1565 (2021).
30. A. Michelson, H. Zhang, S. Xiang, O. Gang, Engineered silicon carbide three-dimensional frameworks through DNA-prescribed assembly. *Nano Lett.* **21**, 1863–1870 (2021).
31. L. Shani, A. N. Michelson, B. Minevich, Y. Fleger, M. Stern, A. Shaulov, Y. Yeshurun, O. Gang, DNA-assembled superconducting 3D nanoscale architectures. *Nat. Commun.* **11**, 1–7 (2020).
32. S. Barany, V. Strelko, Laws and mechanism of adsorption of cations by different ion-exchange forms of silica gel. *Adsorption* **19**, 769–776 (2013).
33. H. I. Akyildiz, M. Lo, E. Dillon, A. T. Roberts, H. O. Everitt, J. S. Jur, Formation of novel photoluminescent hybrid materials by sequential vapor infiltration into polyethylene terephthalate fibers. *J. Mater. Res.* **29**, 2817–2826 (2014).
34. A. Rahman, P. W. Majewski, G. Doerk, C. T. Black, K. G. Yager, Non-native three-dimensional block copolymer morphologies. *Nat. Commun.* **7**, 13988 (2016).
35. A. Subramanian, G. Doerk, K. Kisslinger, D. H. Yi, R. B. Grubbs, C.-Y. Nam, Three-dimensional electroactive ZnO nanomesh directly derived from hierarchically self-assembled block copolymer thin films. *Nanoscale* **11**, 9533–9546 (2019).
36. A. Subramanian, N. Tiwale, G. Doerk, K. Kisslinger, C.-Y. Nam, Enhanced hybridization and nanopatterning via heated liquid-phase infiltration into self-assembled block copolymer thin films. *ACS Appl. Mater. Interfaces* **12**, 1444–1453 (2020).
37. A. Subramanian, N. Tiwale, W.-I. Lee, C.-Y. Nam, Templating functional materials using self-assembled block copolymer thin-film for nanodevices. *Front. Nanotechnol.* **3**, 1 (2021).
38. A. Subramanian, N. Tiwale, C.-Y. Nam, Review of recent advances in applications of vapor-phase material infiltration based on atomic layer deposition. *JOM* **71**, 185–196 (2019).
39. Y. Yu, Z. Li, Y. Wang, S. Gong, X. Wang, Sequential infiltration synthesis of doped polymer films with tunable electrical properties for efficient triboelectric nanogenerator development. *Adv. Mater.* **27**, 4938–4944 (2015).
40. A. Subramanian, N. Tiwale, W. I. Lee, K. Kisslinger, M. Lu, A. Stein, J. Kim, C. Y. Nam, Vapor-phase infiltrated organic-inorganic positive-tone hybrid photoresist for extreme UV lithography. *Adv. Mater. Interfaces* **10**, 2300420 (2023).
41. Y.-C. Tseng, Q. Peng, L. E. Ocola, D. A. Czaplewski, J. W. Elam, S. B. Darling, Enhanced polymeric lithography resists via sequential infiltration synthesis. *J. Mater. Chem.* **21**, 11722–11725 (2011).
42. N. Tiwale, A. Subramanian, K. Kisslinger, M. Lu, J. Kim, A. Stein, C.-Y. Nam, Advancing next generation nanolithography with infiltration synthesis of hybrid nanocomposite resists. *J. Mater. Chem. C* **7**, 8803–8812 (2019).
43. N. Tiwale, A. Subramanian, G. Freychet, E. Gann, K. Kisslinger, M. Lu, A. Stein, J. Kim, C.-Y. Nam, Hybrid resist synthesis by ex-situ vapor-phase infiltration of metal oxides into conventional organic resists, in *Advances in Patterning Materials and Processes XXXVIII* (SPIE, 2021), vol. 11612, pp. 37–42.
44. S. Greil, A. Rahman, M. Liu, C. T. Black, Gas transport selectivity of ultrathin, nanoporous, inorganic membranes made from block copolymer templates. *Chem. Mater.* **29**, 9572–9578 (2017).
45. K. J. Dusoe, X. Ye, K. Kisslinger, A. Stein, S.-W. Lee, C.-Y. Nam, Ultrahigh elastic strain energy storage in metal-oxide-infiltrated patterned hybrid polymer nanocomposites. *Nano Lett.* **17**, 7416–7423 (2017).
46. M. Moshonov, G. L. Frey, Directing hybrid structures by combining self-assembly of functional block copolymers and atomic layer deposition: A demonstration on hybrid photovoltaics. *Langmuir* **31**, 12762–12769 (2015).
47. E. Barry, A. U. Mane, J. A. Libera, J. W. Elam, S. B. Darling, Advanced oil sorbents using sequential infiltration synthesis. *J. Mater. Chem. A* **5**, 2929–2935 (2017).
48. A. Subramanian, N. Tiwale, K. Kisslinger, C.-Y. Nam, Reduced stochastic resistive switching in organic-inorganic hybrid memristors by vapor-phase infiltration. *Adv. Electron. Mater.* **8**, 2200172 (2022).
49. C.-Y. Nam, A. Stein, K. Kisslinger, C. T. Black, Electrical and structural properties of ZnO synthesized via infiltration of lithographically defined polymer templates. *Appl. Phys. Lett.* **107**, 203106 (2015).
50. C.-Y. Nam, A. Stein, Extreme carrier depletion and superlinear photoconductivity in ultrathin parallel-aligned ZnO nanowire array photodetectors fabricated by infiltration synthesis. *Adv. Opt. Mater.* **5**, 1700807 (2017).
51. Y. She, E. D. Goodman, J. Lee, B. T. Diroll, M. Cargnello, E. V. Shevchenko, D. Berman, Block-co-polymer-assisted synthesis of all inorganic highly porous heterostructures with highly accessible thermally stable functional centers. *ACS Appl. Mater. Interfaces* **11**, 30154–30162 (2019).
52. B. K. Barick, A. Simon, I. Weisbord, N. Shomrat, T. Segal-Peretz, Tin oxide nanostructure fabrication via sequential infiltration synthesis in block copolymer thin films. *J. Colloid Interface Sci.* **557**, 537–545 (2019).
53. D. Berman, E. Shevchenko, Design of functional composite and all-inorganic nanostructured materialsviainfiltration of polymer templates with inorganic precursors. *J. Mater. Chem.* **8**, 10604–10627 (2020).
54. J. Chai, D. Wang, X. Fan, J. M. Buriak, Assembly of aligned linear metallic patterns on silicon. *Nat. Nanotechnol.* **2**, 500–506 (2007).
55. C. Cummins, D. Borah, S. Rasappa, A. Chaudhari, T. Ghoshal, B. M. D. O'Driscoll, P. Carolan, N. Petkov, J. D. Holmes, M. A. Morris, Self-assembly of polystyrene-block-poly(4-vinylpyridine) block copolymer on molecularly functionalized silicon substrates: Fabrication of inorganic nanostructured etchmask for lithographic use. *J. Mater. Chem. C* **1**, 7941–7951 (2013).
56. C. Cummins, A. Gangnaik, R. A. Kelly, D. Borah, J. O'Connell, N. Petkov, Y. M. Georgiev, J. D. Holmes, M. A. Morris, Aligned silicon nanofins via the directed self-assembly of PS-b-P4VP block copolymer and metal oxide enhanced pattern transfer. *Nanoscale* **7**, 6712–6721 (2015).
57. T. Ghoshal, A. Chaudhari, C. Cummins, M. T. Shaw, J. D. Holmes, M. A. Morris, Morphological evolution of lamellar forming polystyrene-block-poly (4-vinylpyridine) copolymers under solvent annealing. *Soft Matter* **12**, 5429–5437 (2016).
58. D. O. Shin, J. H. Mun, G.-T. Hwang, J. M. Yoon, J. Y. Kim, J. M. Yun, Y.-B. Yang, Y. Oh, J. Y. Lee, J. Shin, K. J. Lee, S. Park, J. U. Kim, S. O. Kim, Multicomponent nanopatterns by directed block copolymer self-assembly. *ACS Nano* **7**, 8899–8907 (2013).
59. W. Jo, K. J. Freedman, M. J. Kim, in *2012 38th Annual Northeast Bioengineering Conference* (NEBEC, 2012), pp. 191–192.
60. Y. Tian, J. R. Lhermitte, L. Bai, T. Vo, H. L. Xin, H. Li, R. Li, M. Fukuto, K. G. Yager, J. S. Kahn, Y. Xiong, B. Minevich, S. K. Kumar, O. Gang, Ordered three-dimensional nanomaterials using DNA-prescribed and valence-controlled material voxels. *Nat. Mater.* **19**, 789–796 (2020).
61. A. Michelson, B. Minevich, H. Emamy, X. Huang, Y. S. Chu, H. Yan, O. Gang, Three-dimensional visualization of nanoparticle lattices and multimaterial frameworks. *Science* **376**, 203–207 (2022).
62. A. V. Naumkin, A. Kraut-Vass, S. W. Gaarenstroom, C. J. Powell. (2012).
63. C. Z. Leng, M. D. Losego, Vapor phase infiltration (VPI) for transforming polymers into organic–inorganic hybrid materials: A critical review of current progress and future challenges. *Mater. Horiz.* **4**, 747–771 (2017).
64. E. K. McGuinness, Y. Liu, R. Ramprasad, M. D. Losego, Quartz crystal microbalance gravimetry measurements of the sorption of trimethylaluminum into polystyrene and poly(methyl methacrylate). *Mater. Chem. Phys.* **294**, 127026 (2023).
65. M. Rocklein, S. George, Temperature-induced apparent mass changes observed during quartz crystal microbalance measurements of atomic layer deposition. *Anal. Chem.* **75**, 4975–4982 (2003).
66. I. Weisbord, N. Shomrat, R. Azoulay, A. Kaushansky, T. Segal-Peretz, Understanding and controlling polymer–organometallic precursor interactions in sequential infiltration synthesis. *Chem. Mater.* **32**, 4499–4508 (2020).
67. C. Wilson, R. Grubbs, S. George, Nucleation and growth during Al_2O_3 atomic layer deposition on polymers. *Chem. Mater.* **17**, 5625–5634 (2005).
68. L. Wang, Y. Zhou, Y. Yang, A. Subramanian, K. Kisslinger, X. Zuo, Y.-C. Chuang, Y. Yin, C.-Y. Nam, M. H. Rafailovich, Suppression of carbon monoxide poisoning in proton exchange membrane fuel cells via gold nanoparticle/titania ultrathin film heterogeneous catalysts. *ACS Appli. Energy Mater.* **2**, 3479–3487 (2019).
69. N. Tiwale, S. P. Senanayak, J. Rubio-Lara, Y. Alaverdyan, M. E. Welland, Optimization of transistor characteristics and charge transport in solution processed ZnO thin films grown from zinc neodecanoate. *Electron. Mater. Lett.* **15**, 702–711 (2019).

70. N. Tiwale, S. P. Senanayak, J. Rubio-Lara, A. Prasad, A. Aziz, Y. Alaverdyan, M. E. Welland, Solution-processed high-performance ZnO nano-FETs fabricated with direct-write electron-beam-lithography-based top-down route. *Adv. Electron. Mater.* **7**, 2000978 (2021).
71. C. Li, J. Lv, Z. Liang, S. Yao, Study on the optical absorption and green emission of ZnO phosphors by varying Al doping contents. *Opt. Mater.* **35**, 586–589 (2013).
72. H. Yan, Ptychographic phase retrieval by proximal algorithms. *New J. Phys.* **22**, 023035 (2020).
73. D. Kazantsev, N. Wadeson, (2020). *Proceedings of the 6th International Conference on Image Formation in X-ray Computed Tomography* (CT 2020), 3–7 August 2020, Regensburg, Germany.

Acknowledgments: This research used Materials Synthesis and Characterization and Electron Microscopy Facilities of the Center for Functional Nanomaterials (CFN), as well as 11-BM complex matter scattering (CMS) and 3-ID HXN beamlines of the National Synchrotron Light Source II (NSLS-II), both of which are the US Department of Energy (DOE), Office of Science User Facilities at Brookhaven National Laboratory under contract no. DE-SC0012704. This research also used the resources of Surface Science Facility in Advanced Science Research Center at the Graduate Center of CUNY. **Funding:** The DNA assembly work was supported by the DOE, the Office of Basic Energy Sciences, grant DE- SC0008772; the inorganic templating was supported by the U.S. Department of Defense, Army Research Office, W911NF-19-1-0395; and the on-chip material integration was supported by the Keck Foundation. **Author contributions:** Conceptualization: A.M., A.S., C.-Y.N., and O.G. Methodology: A.M., A.S., and N.T. Investigation: A.M., A.S., K.K., J.S.K., D.N., H.Y., E.S., and S.X. Visualization: A.M., A.S., and K.K. Supervision: C.-Y.N. and O.G. Writing—original draft: A.M. and A.S. Writing—review and editing: A.M., A.S., C.-Y.N., and O.G. **Competing interests:** A.M., A.S., C.-Y.N., and O.G. are coinventors on a pending patent application related to this work. The authors declare that they have no other competing interests. **Data and materials availability:** Tomography data files will be available via Zenodo DOI: http://dx.doi.org/10.5281/zenodo.10120663. All data needed to evaluate the conclusions in the paper are present in the paper and/or the Supplementary Materials.

Submitted 28 September 2023
Accepted 5 December 2023
Published 10 January 2024
10.1126/sciadv.adl0604